

AN EXTREME HIGH-VELOCITY BIPOLAR OUTFLOW IN THE PRE-PLANETARY NEBULA IRAS 08005-2356

R. SAHAI¹ & N.A. PATEL²

Draft version October 20, 2018

ABSTRACT

We report interferometric mapping of the bipolar pre-planetary nebula IRAS 08005-2356 (I08005) with an angular-resolution of $\sim 1''$ – $5''$, using the Submillimeter Array (SMA), in the ^{12}CO J=2–1, 3–2, ^{13}CO J=2–1 and SiO J=5–4 ($v=0$) lines. Single-dish observations, using the SMT 10-m, were made in these lines as well as in the CO J=4–3 and SiO J=6–5 ($v=0$) lines. The lines profiles are very broad, showing the presence of a massive ($> 0.1 M_{\odot}$), extreme high-velocity outflow ($V \sim 200 \text{ km s}^{-1}$) directed along the nebular symmetry axis derived from the HST imaging of this object. The outflow’s scalar momentum far exceeds that available from radiation pressure of the central post-AGB star, and it may be launched from an accretion disk around a main-sequence companion. We provide indirect evidence for such a disk from its previously published, broad $\text{H}\alpha$ emission profile, which we propose results from $\text{Ly}\beta$ emission generated in the disk followed by Raman-scattering in the innermost regions of a fast, neutral wind.

Subject headings: circumstellar matter – planetary nebulae: individual (IRAS 08005-2356) – accretion disks – stars: AGB and post-AGB – stars: mass loss – stars: winds, outflows

1. INTRODUCTION

Following the ejection of half or more of their mass via isotropic, slowly expanding winds, AGB stars evolve into planetary nebulae (PNe), which, surprisingly show a diverse range of aspherical (e.g., bipolar and multipolar) morphologies (e.g., Sahai & Trauger 1998, Sahai, Morris & Villar 2011a). Studies of pre-Planetary nebulae (PPNs), objects in transition between the AGB and planetary nebula (PN) evolutionary phases, are critical for characterising the physical processes responsible for this dramatic transformation. Sahai & Trauger (1998) proposed that fast collimated outflows or jets, operating during the PPN and/or very late AGB phase, are the primary agents for the dramatic change in the mass-loss geometry and dynamics during the AGB-to-PN evolutionary phase. However, the physical mechanism for producing these fast outflows remains a mystery. High-angular-resolution interferometric (sub)millimeter-wave observations are the best way to quantitatively probe the fast outflow’s dynamics and energetics – crucial information for theoretical models (e.g., Akashi & Soker 2013), and detailed numerical hydrodynamical simulations (e.g., Lee & Sahai 2003, Balick et al. 2013), for PN shaping.

Such observations have resulted in the discovery of a handful of “extreme-outflow” PPNs – objects in which the molecular outflows reach speeds in excess of $\sim 100 \text{ km s}^{-1}$, e.g., Boomerang Nebula (Sahai et al. 2013), IRAS 22036+5306 (Sahai et al. 2006), IRAS 19374+2359 (Sánchez Contreras et al. 2013), IRAS 16342-3814 (Imai et al. 2012) and HD 101584 (Olofsson et al. 2015). Detailed studies of such extreme objects are likely to provide the best motivation for, and most stringent tests of, theoretical models to

explain their origin (e.g., Blackman & Lucchini 2014).

In this Letter, we report (sub)millimeter-line observations of the PPN IRAS 08005-2356 (I08005), which clearly reveal it to be an extreme-outflow PPN. Early CO J=2–1 observations by Hu et al. (1994) resulted in the marginal detection of a weak, broad line. I08005’s F5Ie central star V510 Pup (Slijkhuis et al. 1991) may have made a recent transition from ejecting oxygen-rich material to carbon-rich material (Bakker et al. 1997). Its morphological classification is $\text{Bo}^*(0.55)$ (Sahai et al. 2007), i.e., it has a bipolar morphology (resolved via HST imaging, Ueta et al. 2000) with lobes open at their ends and a central star seen at $0.55 \mu\text{m}$. Its optical spectrum reveals the presence of a prominent $\text{H}\alpha$ emission line with very broad wings ($\text{FWZI} \sim 2400 \text{ km s}^{-1}$) and a P-Cygni type blue-shifted absorption feature (Sánchez Contreras et al. 2008: SCetal08; also Slijkhuis et al. 1991, Klochkova & Chentsov 2004). Its estimated distance ranges between 2.85 kpc (Oppenheimer et al. 2005: OBS05) and 3–4 kpc (Klochkova & Chentsov 2004); we adopt a value of 3 kpc.

2. OBSERVATIONS

The 1.3 mm and 0.87 mm interferometric observations were obtained with the Submillimeter Array (SMA³) at Mauna Kea, Hawaii. Bandpass calibration was performed using observations of 3C279. At 1.3 (0.87) mm, complex gain calibration was obtained from observations of the quasars 0750+125 and 0730-116 (0747-331 and 0826-225), and flux calibration was obtained from observations of Callisto (Europa). Additional observing parameters are listed in Table 1.

SMA data were calibrated using the MIR-IDL package⁴, and images were made using the Miriad software. Data cubes were obtained with a velocity resolution

raghvendra.sahai@jpl.nasa.gov

¹ Jet Propulsion Laboratory, MS 183-900, California Institute of Technology, Pasadena, CA 91109

² Harvard-Smithsonian Center for Astrophysics, Cambridge

³ The Submillimeter Array is a joint project between the Smithsonian Astrophysical Observatory and the Academia Sinica Institute of Astronomy and Astrophysics and is funded by the Smithsonian Institution and the Academia Sinica

⁴ <http://www.cfa.harvard.edu/~cqi/mircook.html>

smoothed to 10 km s^{-1} per channel (to increase the S/N in each channel). Natural weighting was used to produce all images.

Single-dish observations of the ^{12}CO J=2–1, 3–2 and 4–3, ^{13}CO J=2–1, and SiO ($v=0$) J=5–4 and 6–5 line emission were obtained at SMT during 2014, Nov/Dec and 2015 Jan. Telescope pointing was frequently checked on VY CMa, and is estimated to be better than a small fraction of the beam. The weather was generally good, with system temperatures in the range $T_{sys} \sim 200 - 250 \text{ K}$ at 1.3 mm and $T_{sys} \sim 1300 \text{ K}$ at 0.7 and 0.8 mm. Linear baselines were subtracted from the spectra shown. We have assumed main-beam efficiency factors of 0.76, 0.66, and 0.62 for the 230.6, 345.8, and 461.0 GHz observations (Edwards et al. 2014).

The optical images were taken with the NASA/ESA Hubble Space Telescope in GO programs ID 6364 (PI: M. Bobrowsky) and 6366 (PI: S. Trammell), using the PC on WFPC2, and extracted from the Hubble Legacy Archive⁵.

3. RESULTS

3.1. Optical Imaging

I08005 shows an hourglass morphology in the HST F439W, F555W, and F675W images (Fig. 1) – the lobes, separated by a narrow dark lane, flare out from the central star’s location, and attain a cylindrical shape. The SE lobe is significantly brighter than the NW one. A narrow, slightly-curved feature of linear extent $0''.38$, is seen extending from the central star in the SE lobe (see inset). The feature is oriented at a $PA = 120^\circ$, slightly different from the PA of the nebula symmetry axis, 143° . The total linear extent of the nebula along its long axis, as seen in the F555W image, is $\sim 2''.6$ ($1.2 \times 10^{17} \text{ cm}$).

3.2. Millimeter-Wave Observations

We detected the CO J=2–1, 3–2 and SiO J=5–4 lines with the SMA. The CO J=3–2 and SiO J=5–4 have significantly lower signal-to-noise, and the ^{13}CO J=2–1 is tentatively detected. The (spatially) integrated SMA CO J=2–1 line profile (using a $15''$ diameter circular aperture) shows a very broad profile (Fig. 2) covering a total velocity extent of about 350 km s^{-1} , i.e., from $-150 \lesssim V_{lsr} (\text{km s}^{-1}) \lesssim 200$. The SMT CO J=2–1 line profile (Fig. 2) is similar to the SMA one (a narrow emission feature at $V_{lsr} = 36 \text{ km s}^{-1}$ due to the presence of an unrelated line-of-sight interstellar cloud, has been removed from the profile by interpolation). A Gaussian fit to the profile gives a central velocity $V_{lsr} \sim 25 \text{ km s}^{-1}$, and a FWHM of 196 km s^{-1} .

We have divided the velocity range spanned by the CO J=2–1 line into three intervals on each side of the central velocity – the extreme high-velocity or EV component (blue: $-150 < V_{lsr} (\text{km s}^{-1}) < -85$, red: $130 < V_{lsr} (\text{km s}^{-1}) < 200$), a medium-velocity or MV component (blue: $-85 < V_{lsr} (\text{km s}^{-1}) < -30$, red: $70 < V_{lsr} (\text{km s}^{-1}) < 130$), and a low-velocity LV component (blue: $-30 < V_{lsr} (\text{km s}^{-1}) < 25$, red: $25 <$

$V_{lsr} (\text{km s}^{-1}) < 75$). The SMA CO J=2–1 emission in the blue and red-shifted parts of the EV, MV, and LV components show separations of about $2''.1$, $1''.1$, $0''.5$, respectively, along the nebular symmetry axis (Fig. 3a).

These results imply the presence of a fast, bipolar outflow with a (roughly) linear velocity-gradient, directed along the nebular symmetry axis, and a linear extent of $\sim 2''.1$. Since AGB mass-loss is typically spherical, with outflow velocities of $10\text{--}15 \text{ km s}^{-1}$, we conclude that the outflow observed in CO J=2–1 emission is a fast, collimated post-AGB outflow, typical of the PPN evolutionary phase. We made similar plots from the SMA data cubes for CO J=3–2 (Fig. 3b) and SiO J=5–4 (not shown), dividing the emission velocity-range into two halves only (blue: $-90 < V_{lsr} (\text{km s}^{-1}) < 20$, red: $30 < V_{lsr} (\text{km s}^{-1}) < 130$) due to the lower S/N in these lines, and found that these show a separation of $0''.85$ roughly along the nebular axis. This separation is equal to that derived from our CO J=2–1 data for the same red and blue outflow-velocity ranges, implying that the SiO outflow’s linear extent is likely comparable to that of CO.

We also detected the CO J=4–3, J=3–2 and ^{13}CO J=2–1 as well as the SiO ($v=0$) J=5–4 and 6–5 lines with the SMT, but with lower S/N (Fig. 2). We have compared the total CO J=2–1 line fluxes from our SMA and SMT data, as these have the highest S/N, and find that these are consistent within 15%, i.e., within typical calibration uncertainties) – we conclude that the SMA data do not suffer from any significant flux losses.

Continuum images were obtained after removing spectral regions containing line emission, using the Miriad task uvlin. No continuum emission was detected from I08005. Using line-free channels, we find a 1σ noise of 1.05 (1.2) mJy/beam in the USB (LSB) at 1.3 mm and 11 (18) mJy/beam in the USB (LSB) at 0.87 mm.

4. THE POST-AGB BIPOLAR OUTFLOW

4.1. Outflow Properties

We now determine the physical properties of the high-velocity bipolar outflow (e.g., scalar momentum, mass, and age) from an analysis of the molecular-line data. The observed ratios of the CO J=2–1, 3–2 and J=4–3 fluxes (in K km s^{-1}) are $1 : 1.27 : 1.2$, which imply corresponding non-beam diluted flux ratios of $1 : R_{32/21} : R_{43/21} = 1 : 0.6 : 0.3$, since the source is unresolved by the SMT beams of $32''$, $22''$, and $16''$ in these lines.

We first make a simple emission model assuming a spherical outflow at a uniform excitation temperature equal to the kinetic temperature, T_{kin} , and carry out a least-squares fit to the line fluxes⁶, varying T_{kin} , the outer radius (R_{out}), and mass of the emitting region (M_g). We find $R_{out} = 1.4''$ and $T_{kin} = 13.6 \text{ K}$. However, the derived T_{kin} is rather low compared to energy of the CO J=4 level (55.4 K), and modeling with the non-LTE RADEX code (van der Taak et al. 2007) shows that the J=4–3 excitation temperature, $T_{ex(43)}$, is lower than T_{kin} by about (20–25)% due to the relatively low CO line optical depths in our model (< 0.01) and the average density, $n_{av} \sim 3.5 \times 10^4 \text{ cm}^{-3}$, implied by the emitting region’s mass and volume. Thus, the resulting,

⁶ derived using the formulation in Olofsson et al. (1990)

⁵ A collaboration between the Space Telescope Science Institute (STScI/NASA), the Space Telescope European Coordinating Facility (ST-ECF/ESA) and the Canadian Astronomy Data Centre (CADC/NRC/CSA)

corrected model $R_{43/21} \sim 0.11$, too low to fit the data.

Using RADEX, we find that the average density required to bring $T_{\text{ex}(43)}$ closer to T_{kin} in order to fit the observed source brightness temperature ratios, is $n_{\text{av}} > 7.5 \times 10^4 \text{ cm}^{-3}$; the required $T_{\text{kin}} = 15.5 \text{ K}$, giving a source size of $2''.4$, comparable to the CO source-size estimated from the SMA data. The model source size is similar to the size derived from the HST image, implying that the CO emission likely comes from the dense walls of the bipolar lobes seen in scattered light. The CO column density is, $N_{\text{CO}} > 5 \times 10^{17} \text{ cm}^{-2}$ (and the J=2-1, 3-2, and 4-3 lines have optical depths of 0.48, 0.44, 0.20). Assuming that the average emitting column is equal to the source radius, we find a CO-to-H₂ abundance ratio of, $f_{\text{CO}} = 1.3 \times 10^{-4}$, in reasonable agreement with the value typically assumed for PPNs, 2×10^{-4} (e.g., Bujarrabal et al. 2001). Assuming a spherical emitting volume, the mass is, $M_{\text{g}} = 0.076 M_{\odot}$. The $^{12}\text{CO}/^{13}\text{CO}$ abundance ratio is, $f(^{12}\text{C}/^{13}\text{C})=9.6$, from fitting the $^{12}\text{CO}/^{13}\text{CO}$ J=2-1 line flux ratio corrected for the different beam-dilutions (8.1).

The above values of M_{g} and $f(^{12}\text{C}/^{13}\text{C})$ are lower limits since this is our “minimum-mass” model – models with higher values of n_{av} are allowed. However, the total mass increases more slowly than the average density, since in models with higher values of n_{av} , the emitting region’s size is smaller. For example, if we use the dust mass, $M_{\text{d}}=0.0019 L_{\odot} (D/2.85 \text{ kpc})^2$ derived by OBS05 from a detailed 2D radiative transfer model of I08005’s SED, scale it to $D=3 \text{ kpc}$, and adopt a typical gas-to-dust ratio for oxygen-rich AGB stars, $M_{\text{g}}/M_{\text{d}} = 200$, we get $M_{\text{g}} = 0.42 M_{\odot}$. For this value of M_{g} , we need a CO model with $n_{\text{av}} \sim 8 \times 10^5 \text{ cm}^{-3}$, a factor ~ 10 higher than in our minimum-mass model; $T_{\text{kin}} = 11.5 \text{ K}$, and $N_{\text{CO}} = 1.6 \times 10^{18} \text{ cm}^{-2}$. Since the CO J=2-1 optical depth is higher ($\tau_{21} = 1.95$), the abundance ratio is higher, $f(^{12}\text{C}/^{13}\text{C})=17$.

We calculate the scalar momentum using the formulation described in Bujarrabal et al. (2001). Using our minimum-mass model, we find $P_{\text{sc}} \sim 2.8 \times 10^{39} \text{ g cm s}^{-1}$ for an inclination angle of the nebular axis to the sky-plane, $i = 30^\circ$ (OBS05). The kinetic energy in the outflow is $E_{\text{kin}} \sim 2.6 \times 10^{45} \text{ erg}$. These values of P_{sc} and E_{kin} lie near the upper end of the range for PPNs, $10^{37-40} \text{ g cm s}^{-1}$ and 10^{42-46} erg (Bujarrabal et al. 2001). This outflow cannot be driven by radiation pressure because the lobes’ dynamical (expansion) time-scale, $t_{\text{dyn}} = 190 \text{ yr}$ (from dividing the model CO shell-size by the CO J=2-1 FWHM line-width) is much smaller than that required by radiation pressure to accelerate the observed bipolar outflow to its current speed, $t_{\text{rad}} = P_{\text{sc}}/(L/c) \sim 6.6 \times 10^4 \text{ yr}$, given I08005’s luminosity of $6980 L_{\odot}$ at $D=3 \text{ kpc}$ (using the value derived by OBS05, $6300(D/2.85 \text{ kpc})^2 L_{\odot}$.) The mass-loss rate in the outflow is $> 5.8 \times 10^{-4} M_{\odot} \text{ yr}^{-1}$.

The observed SMT SiO J=6-5 to 5-4 line flux ratio is 0.94 (with about $\pm 15\%$ uncertainty), implying an intrinsic flux ratio (i.e., corrected for beam-dilution) of $R(\text{SiO})_{65/54} = 0.66$, since the source is unresolved by the SMT beams of $34''$ and $28''.4$ in these lines. Using RADEX, we find that for $T_{\text{kin}} = 15.5 \text{ K}$, the average H₂ density in the SiO emission region is, $n_{\text{av}} > 2 \times 10^5 \text{ cm}^{-3}$

in order to fit the observed value of $R(\text{SiO})_{65/54}$. The fractional SiO abundance is $\sim 4 \times 10^{-5}$, close to the maximum value assuming cosmic abundances (6×10^{-5}), and comparable to the observed maximum circumstellar SiO abundance in oxygen-rich AGB stars ($few \times 10^{-5}$: Sahai & Biegging 1993). If the SiO emission comes from shocked gas at a higher kinetic temperature than that for CO, the minimum density required is higher.

4.2. A Central Accretion Disk?

Evidence of very fast outflows in I08005 comes from three independent probes: (i) CO data (presented here), (ii) H α spectrum in SCetal08, and (iii) OH maser emission (VLA mapping) reported in Zijlstra et al. (2001). The OH maser features cover the velocity range of $0 < V_{\text{lsr}} (\text{km s}^{-1}) < 100$, i.e., roughly the range covered by red half of the CO J=2-1 profile. In contrast to OH and CO emission, the H α absorption probes atomic gas. Since the H α absorption feature is not spatially resolved in the ground-based long-slit spectra, it is difficult to directly establish its relationship to the fast molecular outflow, however the close agreement between the terminal outflow velocities derived for these indicates that they are closely associated. The atomic gas may be located inside the lobes and may constitute unshocked material of an underlying jet, and/or the interface between the latter and the lobe walls, as proposed for IRAS 22036+5306 (Scetal06). The jet-like feature seen in the HST image (Fig. 1, inset) may represent the precessing jet’s signature close to its launch-site.

The high-speed bipolar outflow in I08005 may be driven by an accretion disk. Bakker et al. (1997) find numerous narrow, double-peaked, chromospheric emission lines from neutral and singly ionized metals, and propose that these might arise in an accretion disk. We conjecture that the broad H α wings seen towards this object might arise as a result of Raman-scattering of Ly β emission generated by such a disk – a process that produces an H α profile with a width that is a factor 6.4 larger than the Ly β width and a λ^{-2} wing profile. The very wide ($FWZI \sim 2400 \text{ km s}^{-1}$) H α line wings in I08005 show this shape, furthermore a weak emission feature around 6830 \AA with $FWZI \sim 150 \text{ km s}^{-1}$, corresponding to Raman-scattering of the 1032 \AA component of the O VI doublet at $\lambda\lambda 1032, 1038$ is also seen (SCetal08); the 7088 \AA feature that corresponds to the 1038 \AA component is a factor 4 weaker, and too weak to be visible.

Other line-broadening mechanisms include electron scattering and emission from a rotating disk. Arrieta & Torres-Peimbert (2003) find that electron scattering requires extreme densities (e.g., $n_e > 10^{12} \text{ cm}^{-3}$ in M 2-9) making that an implausible mechanism. Keplerian rotation in a disk around the central star is too low to directly account for the broad line-width in I08005 (and PPNe in general: Sahai et al. 2011b) – taking the radius for the central post-AGB star of I08005 to be $R \sim 50 R_{\odot}$ (Slijkhuis et al. 1991) and a nominal stellar mass of $1 M_{\odot}$, we find the maximum rotation speed is $V_{\text{max}} < 56.5 \text{ km s}^{-1}$, too low for generating the extreme line-wings of the H α profile, even with the factor 6.4 increase provided by Raman-scattering. We therefore conclude that the accretion disk in I08005 must be around a much smaller star, e.g., a main-sequence companion.

The Raman-scattering likely occurs in the innermost regions of the fast neutral wind seen via its blue-shifted absorption feature signature in the H α profile. In this case, following Sahai et al. (2011b), we scale from the minimum scattering column density, $N_s = 10^{19-20} \text{ cm}^{-2}$ needed to achieve the Raman conversion efficiency necessary for producing the very broad observed line-widths (see Fig.1 of Lee & Hyung 2000), to find that $dM_s/dt > (0.35 - 3.5) \times 10^{-8} M_\odot \text{ yr}^{-1} (r_w/30 \text{ AU}) (D/3 \text{ kpc}) (V_{exp}/100 \text{ km s}^{-1}) (N_s/10^{19} \text{ cm}^{-2})$, where r_w is the radius of the neutral wind where the Raman-scattering occurs. V_{exp} is set equal to $0.5 \times FWHM$ of the broad CO J=2-1 line profile, and similar to the neutral outflow's average outflow-velocity derived by SCetal08. The mass-loss rate requirement is easily met in I08005 since OBS05 derive a mass-loss rate of $4.4 \times 10^{-6} M_\odot \text{ yr}^{-1}$ for a collimated fast wind in the 24-780 AU region around the central star,

5. DISCUSSION

I08005 is very similar to other extreme-outflow oxygen-rich PPNs, IRAS 22036+5306 (Sahai et al. 2006) and HD 101584 (Olofsson et al. 2015, Sivarani et al. 1999) in the properties of its collimated fast outflow (expansion-velocity, scalar-momentum, and kinetic-energy), and its H α emission profile (very broad wings, P-Cygni absorption). But in striking contrast to these objects, it appears to lack mm and submm continuum emission from its central region – the ratio of its 1.3 mm to 60 micron flux is $< 10^{-4}$ (3σ), compared to 0.6×10^{-3} and 1.5×10^{-3} for HD 101584 and IRAS 22036+5306, respectively.

Both PPNs, as well as the “disk-prominent” sub-class of young post-AGB objects (dpAGB objects: Sahai et al. 2011c), which unlike PPNs, show little or no extended nebulosity, and have central stars that are radial-velocity binaries (e.g., van Winckel et al. 2008), emit relatively strong mm/submm continuum emission from their cen-

tral regions. This emission has been attributed to the presence of substantial masses of cool, mm-sized grains (Sahai et al. 2011c, Gielen et al. 2007, de Ruyter et al. 2006). Their origin is not understood at present but is potentially a key probe of important mass-ejection processes occurring during the late-AGB and post-AGB evolutionary phases, especially those that lead to the formation of large dusty equatorial disks or torii. For example, in HD 101584, where a binary companion has been found from radial-velocity variations (Bakker et al. 1997), Olofsson et al. (2015) propose a scenario in which both the formation of the central, equatorially-dense mass structure and the collimated outflow result from a common-envelope (CE) event – but the latter does not release enough energy to drive the mass-ejection, and another mechanism augments or even dominates it.

The apparent lack of a substantial mass of material in the equatorial waist of I08005 suggests that perhaps it did not undergo a CE event, and its collimated outflow (and collimated outflows in PPNs generally) may be launched differently, possibly from an accretion disk as we have suggested earlier. I08005 is thus a key post-AGB object for further detailed study. For example, ALMA can be used to probe its compact central region, in order to search for weak mm/submm continuum emission that may be present but was below our sensitivity limit, and for the presence of gas (and its kinematics) associated with its dusty waist.

We thank Ken Young and Ray Blundell for granting filler time on the SMA. R.S. is thankful for partial financial support for this work from a NASA/ ADP and LTSA grant. R.S.'s contribution to this paper was carried out at JPL, California Institute of Technology, under a contract with NASA.

REFERENCES

- Akashi, M., & Soker, N. 2013, MNRAS, 436, 1961
 Arrieta, A., & Torres-Peimbert, S. 2003, ApJS, 147, 97
 Bakker, E. J., van Dishoeck, E. F., Waters, L. B. F. M., & Schoenmaker, T. 1997, A&A, 323, 469
 Balick, B., Huarte-Espinoso, M., Frank, A., et al. 2013, ApJ, 772, 20
 Blackman, E. G., & Lucchini, S. 2014, MNRAS, 440, L16
 Bujarrabal, V., Castro-Carrizo, A., Alcolea, J., & Sánchez Contreras, C. 2001, A&A, 377, 868
 de Ruyter, S., Van Winckel, H., Maas, T. et al. 2006, A&A, 448, 641
 Edwards, S. et al. 1987, ApJ, 321, 473
 Edwards, J. L., Cox, E. G., & Ziurys, L. M. 2014, ApJ, 791, 79
 Gielen, C., van Winckel, H., Waters, L. B. F. M., Min, M., & Dominik, C. 2007, A&A, 475, 629
 Hu, J. Y., te Lintel Hekkert, P., Slijkhuis, F., et al. 1994, A&AS, 103, 301
 Imai, H., Chong, S. N., He, J.-H., et al. 2012, PASJ, 64, 98
 Klochkova, V. G., & Chentsov, E. L. 2004, Astronomy Reports, 48, 301
 Lee, H.-W., & Hyung, S. 2000, ApJ, 530, L49
 Lee, C.-F., & Sahai, R. 2003, ApJ, 586, 319
 Olofsson, H., Vlemmings, W. H. T., Maercker, M., et al. 2015, A&A, 576, L15
 Olofsson, H., Carlstrom, U., Eriksson, K., Gustafsson, B., & Willson, L. A. 1990, A&A, 230, L13
 Oppenheimer, B. D., Biegging, J. H., Schmidt, G. D., Gordon, K. D., Misselt, K. A., & Smith, P. S. 2005, ApJ, 624, 957
 Sahai, R., & Biegging, J. H. 1993, AJ, 105, 595
 Sahai, R., Claussen, M. J., Schnee, S., Morris, M. R., & Sánchez Contreras, C. 2011c, ApJ, 739, L3
 Sahai, R., Morris, M. R., & Villar, G. G. 2011a, AJ, 141, 134
 Sahai, R., Sánchez Contreras, C., Morris, M. R., & Claussen, M. 2011b, Asymmetric Planetary Nebulae 5 Conference, 11
 Sahai, R., Morris, M., Sánchez Contreras, C., & Claussen, M. 2007, AJ, 134, 2200
 Sahai, R. & Trauger, J.T. 1998, AJ, 116, 1357
 Sahai, R., Vlemmings, W. H. T., Huggins, P. J., Nyman, L.-Å., & Gonidakis, I. 2013, ApJ, 777, 92
 Sahai, R., Young, K., Patel, N. A., Sánchez Contreras, C., & Morris, M. 2006, ApJ, 653, 1241
 Sivarani, T., Parthasarathy, M., García-Lario, P., Machado, A., & Pottasch, S. R. 1999, A&AS, 137, 505
 Skopal, A. 2006, A&A, 457, 1003
 Slijkhuis, S., de Jong, T., & Hu, J. Y. 1991, A&A, 248, 547
 Sánchez Contreras, C., Martin, S., & Sahai, R. 2013, *Highlights of Spanish Astrophysics VII*, Eds.: J.C. Guirado, L.M. Lara, V. Quilis, and J. Gorgas., 671
 Sánchez Contreras, C., Sahai, R., Gil de Paz, A., & Goodrich, R. 2008, ApJS, 179, 166
 van der Tak, F.F.S., Black, J.H., Schoier, F.L., Jansen, D.J., van Dishoeck, E.F., 2007, A&A 468, 627
 Ueta, T., Meixner, M., & Bobrowsky, M. 2000, ApJ, 528, 861
 van Winckel, H., Deroo, P., Gielen, C., et al. 2008, Evolution and Nucleosynthesis in AGB Stars, AIP Conference Proceedings, 1001, 349

TABLE 1
SMA OBSERVATIONAL PARAMETERS

Lines	Freq. Range [GHz]	$\Delta\nu$ [kHz]	Array (# Ants.)	Time ¹ [hr]	Beam, PA " \times ", $^\circ$	T_{sys} [K]	Epoch yy/mm/dd
¹² CO(2-1) continuum ³	USB ² : 228.85–232.85 228.9–229.6, 229.9–230.2 230.8–232.9	812.5	compact (6)	1	4.99×2.73 , 20.8	100–230	13/12/11
¹³ CO, C ¹⁸ O(2-1) SiO(5-4), v=0 continuum ³	LSB ² : 216.85–220.85 216.9–217.0, 217.3–219.4
¹² CO(3-2) continuum ³	LSB ² : 342.0–346.0 342.0–345.4	812.5	extended (7)	2	0.85×0.56 , 33.5	240–400	14/04/13
continuum ³	USB ² : 354.0–358.0

^aOn-source integration time

^bThe frequency range for the full spectrometer passband covering line and continuum regions

^cThe frequency ranges used for extracting the continuum

Zijlstra, A. A., Chapman, J. M., te Lintel Hekkert, P., Likkell, L.,
Comeron, F., Norris, R. P., Molster, F. J., & Cohen, R. J. 2001,
MNRAS, 322, 280

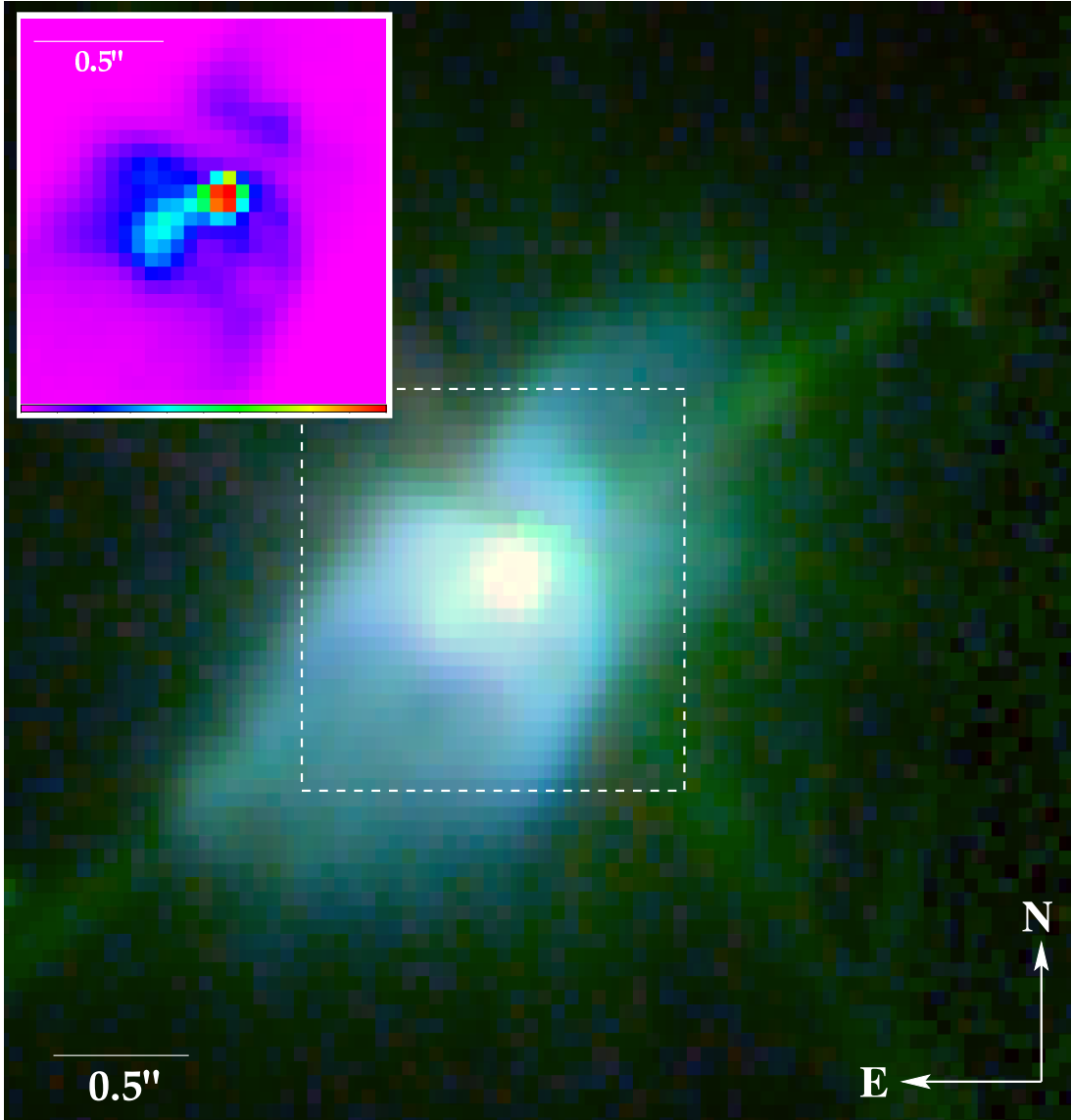


FIG. 1.— HST color-composite (red: F675W, green: F555W, blue: F439W) image of I08005 (log stretch). Panel size is $3''.94 \times 3''.94$. The diagonal linear features are diffraction spikes due to the bright central source in the relatively long-exposure F555W image. Inset is a false-color view (linear stretch: colorbar shows counts/s from 0 to 210) of the central $1''.4 \times 1''.4$ region (dashed box) in F439W, highlighting the curved jet-like feature emanating from the central source.

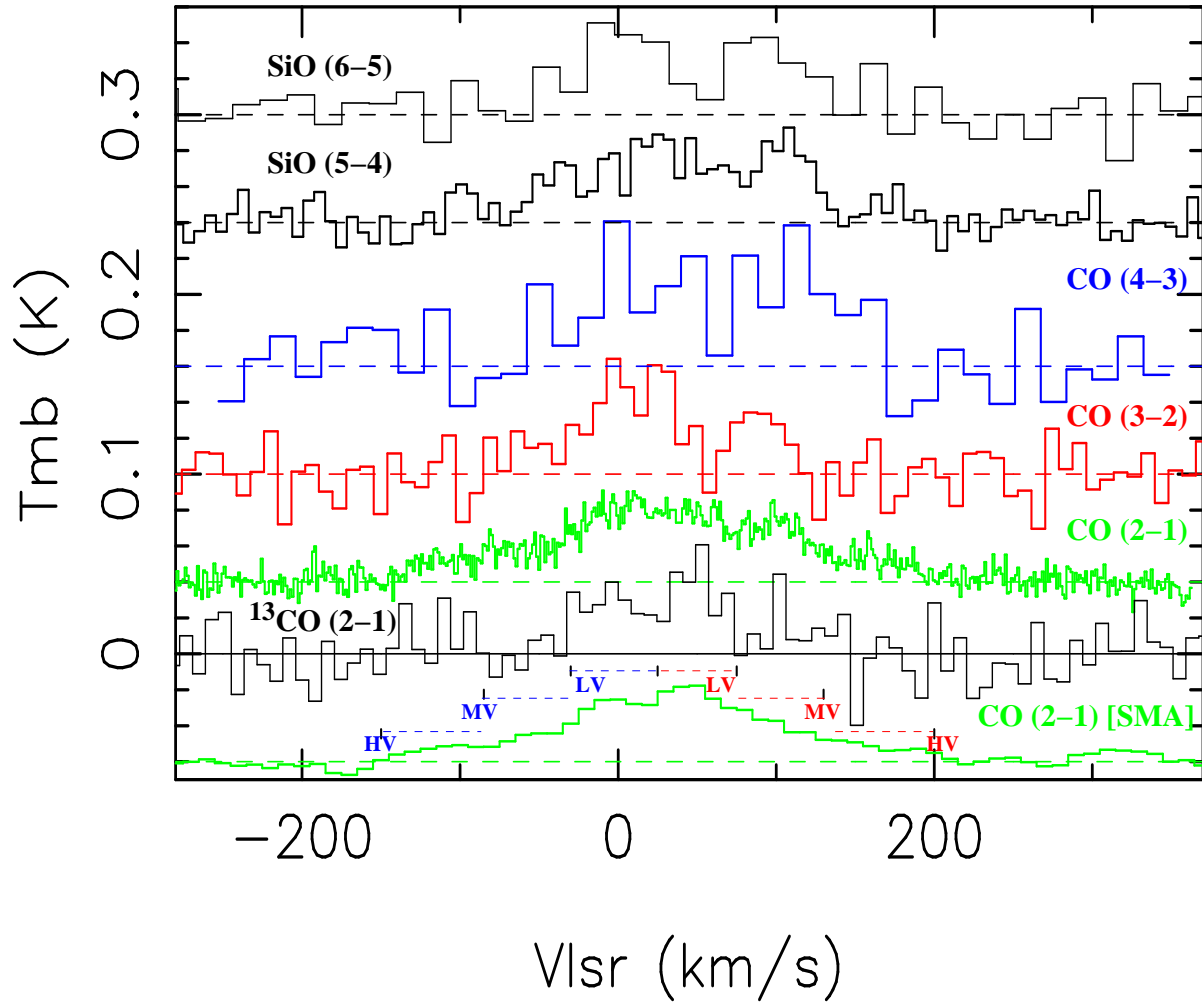


FIG. 2.— Molecular-line emission from I08005. The SMT spectra (shown above $T_{mb} = 0$ axis) have been shifted vertically for clarity, after scaling as follows: SiO $J=6-5$ and $J=5-4$ ($\times 4$), ^{12}CO $J=4-3$ and $2-1$ ($\times 2$), & ^{13}CO $J=2-1$ ($\times 10$). The velocity ranges of the HV, MV, & LV components are marked in the SMA panel. The SMA ^{12}CO $J=2-1$ spectrum, shifted below $T_{mb} = 0$, shows the total flux divided by the SMT conversion factor of 44.5 Jy/K, then scaled $\times 2$, for comparison with the SMT spectrum. The apparent difference in the SMT and SMA CO $J=2-1$ line-profiles at $V_{lsr} \sim 100 \text{ km s}^{-1}$ is probably due to non-linear baseline structure that is not removed by the linear baseline subtraction.

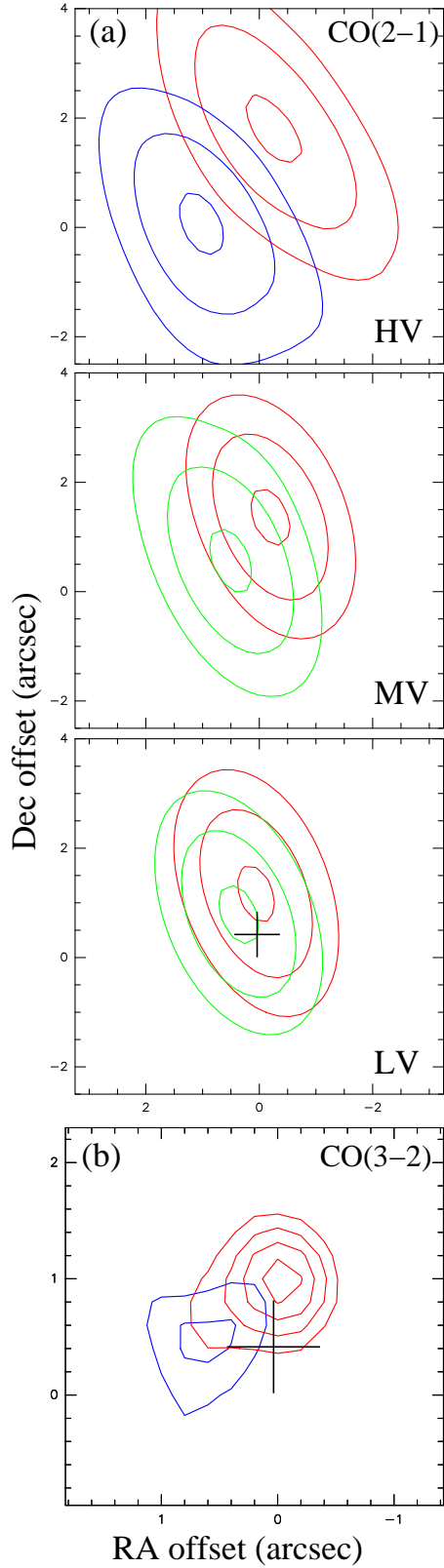


FIG. 3.— SMA CO emission integrated over different velocity (V_{lsr}) ranges (a) J=2-1, (*top*) blue: -150, -85, red: 130, 200; (*middle*) blue: -85, -30, red: 70, 130; (*bottom*) blue: -30, 25, red: 25, 75. (b) J=3-2, blue: -90, 20, red: 30, 130. Contour levels for CO J=2-1 (3-2) are: minimum=50 (46)%, step=10 (15)% of the peak intensities. The central source in the HST image (marked with a cross), is offset ($0''.041, 0''.4$) relative to the phase-center (at 0,0 with J2000 coordinates RA=08:02:40.7, Dec=-24:04:43.0), and consistent with the bipolar-outflow center, within the combined $1-\sigma$ uncertainty, $\sim(\pm 0''.4, \pm 0''.4)$, of the absolute HST and SMT astrometry.